# A three-phase free boundary problem with melting ice and dissolving gas

MAURIZIO CESERI[1] and JOHN M. STOCKIE[2]

[1]*Istituto per le Applicazioni del Calcolo "M. Picone", CNR,
via dei Taurini 19, 00185 Roma, Italy*
*email*: m.ceseri@iac.cnr.it
[2]*Department of Mathematics, Simon Fraser University, 8888 University Drive, Burnaby,
British Columbia, Canada, V5A 1S6*
*email*: jstockie@sfu.ca

We develop a mathematical model for a three-phase free boundary problem in one dimension that involves interactions between gas, water and ice. The dynamics are driven by melting of the ice layer, while the pressurized gas also dissolves within the meltwater. The model incorporates the Stefan condition at the water–ice interface along with Henry's law for dissolution of gas at the gas–water interface. We employ a quasi-steady approximation for the phase temperatures and then derive a series solution for the interface positions. A non-standard feature of the model is an integral free boundary condition that arises from mass conservation owing to changes in gas density at the gas–water interface, which makes the problem non-self-adjoint. We derive a two-scale asymptotic series solution for the dissolved gas concentration, which because of the non-self-adjointness gives rise to a Fourier series expansion in eigenfunctions that do not satisfy the usual orthogonality conditions. Numerical simulations of the original governing equations are used to validate series approximations.

**Key words:** Free boundaries; Stefan problem; Gas dissolution; Asymptotic analysis; Multiscale; Multiphysics

## 1 Introduction

This paper is concerned with a three-phase free boundary problem involving interactions between ice, liquid water and air. The water–ice interface is driven by a melting process, while the gas–water interface is governed by the dissolution of gas within the water phase. The primary phenomenon we are interested in capturing is the compression or expansion of gas that occurs in response to the motion of phase interfaces.

Free boundaries arise naturally in the study of phase change problems and have been the subject of extensive study in the applied mathematics literature [6, 10, 11, 13]. Mathematical models of the free boundaries generally involve solving partial differential equations on some region(s) along with given boundary conditions on a portion of the boundary; however, part of the domain boundary remains unknown, and thus some additional relationship must be provided to determine the free boundary. A classical example is the Stefan problem for a solid–liquid interface [6] that describes a melting or solidification process. Here the primary variable (temperature) is governed by a diffusion

equation, while the speed of the solid–liquid interface is related to the difference in heat flux on either side, which is a statement of conservation of energy. Friedman [8] established well-posedness and regularity results for this melting problem, while Crank [6] and Carslaw and Jaeger [2] derived analytical solutions using Neumann's method for a variety of physical applications. A characteristic feature of all of these solutions is that the speed of the free boundary between the phases is proportional to $t^{1/2}$, where $t$ is the elapsed time.

Another class of free boundary problems occurs in the study of dissolution and cavitation of gas bubbles immersed in fluid [22]. Friedman [9] studied the evolution of a spherically symmetric bubble immersed in a water-filled container of infinite extent and proved existence, uniqueness and regularity of the solution. Keller [16] studied a similar problem and determined the conditions under which multiple gas bubbles are stable. In particular, he found that in an infinite medium, gas bubbles should either collapse or else grow indefinitely. In a closed container, however, bubbles can reach a stable equilibrium state, and he proved that the only stable solution is that with a single bubble.

This paper was motivated by a recent modelling study of sap exudation in maple trees during the spring thaw [3]. Exudation is the process whereby maple trees (and other related species) generate positive stem pressure that causes sap to seep out of any hole bored in the trunk. In late winter there are no leaves to drive transpiration and the maple tree's internal pressure generation mechanism is believed to derive from thawing of frozen sap within libriform fibre cells located in the sapwood or xylem [20]. These fibres are typically filled with gas during the growing season, but during the onset of winter, ice is believed to form on the inner fibre walls, thereby compressing the gas trapped inside. During the spring thaw, the ice layer melts and releases the compressed gas, which is then free to re-pressurise the sap. A mathematical model for sap exudation has been developed recently in Ceseri and Stockie [3], which contains more details about the physical processes at the cellular scale. This microscale model predicts buildup of stem pressures sufficient to dissolve gas bubbles in the xylem sap, which may also be related to the phenomenon of winter embolism recovery that occurs in a much wider range of tree species [18, 26].

In this paper we consider a mathematical model for a simpler situation in which a closed container (analogous to a xylem cell) is divided into three compartments containing gas, water and ice, in that order. While this scenario is not the same as that in maple, it is nonetheless similar enough that it permits us to study in detail the dynamics of the free boundaries. To our knowledge there has been no other similar study of three-phase flow involving gas dissolution and ice melting. There are several other problems arising in porous media flow that have some of the same features as our model. For example, the modelling of marine gas hydrates [25, 28] involves an interplay between gaseous and solid hydrates, water and possibly other components flowing within porous sediments. Although these models involve the Stefan condition for a melting front, the gas dynamics are driven by hydrate dissociation instead of gas dissolution. Another related problem arises in the freezing and thawing of soils contaminated by non-aqueous phase liquids (or NAPLs) [15, 23]. Here, there is a dissolved gas component, but the problem is complicated by the presence of additional phases as well as effects such as mixed wettability.

The purpose of the present work is to analyse a simple three-phase model that incorporates the dynamics of melting and dissolution. The model is introduced in Section 2
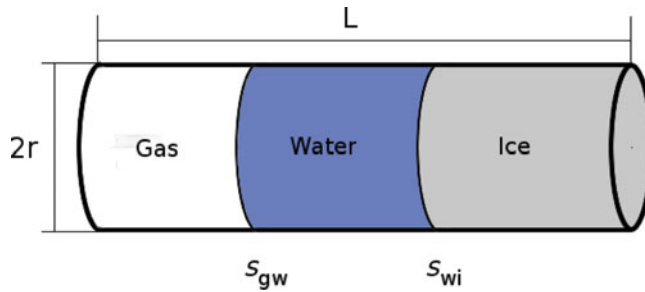
FIGURE 1. (Colour online) Diagram depicting the cylindrical geometry and moving phase interfaces.

and reduced to non-dimensional form. A numerical algorithm is described in Section 3, and simulations in Section 4 yield insight into the behaviour of the solution. Motivated by these results, we then derive an asymptotic solution in Section 5 that captures the essential dynamics, and comparisons are drawn with the full numerical solution. Our main aim in this work is three-fold:

- To understand the basic phase interface dynamics and identify relevant dimensionless quantities and time scales.
- To develop approximate analytical solutions that can be used either to design more efficient numerical schemes or to upscale material coefficients for microscale models such as [3].
- To draw connections with existing results on bubble dissolution dynamics.

## 2 Mathematical model

Consider a cylindrical container of constant radius $r$ and length $L$ (both measured in metres) that is separated into three compartments containing gas, water and ice as pictured in Figure 1. Assume that the cylinder is long and thin so that $L \gg r$ and we can restrict ourselves to a one-dimensional setting where the axial coordinate $x$ varies from 0 to $L$. There are two moving interfaces at locations $x = s_{gw}(t)$ and $s_{wi}(t)$ that separate gas from water and water from ice respectively.

For the sake of simplicity, we consider melting driven by a heat source applied on the left-hand boundary; although we do not consider the freezing process, our model can be easily extended to handle freezing. We are thus interested in the following physical phenomena: (1) heat transfer within and between the three phases; (2) phase change at the water–ice interface as ice melts to form liquid water and (3) dissolution of pressurised of gas at the gas–water interface, with subsequent diffusion of dissolved gas in the water compartment. The moving boundaries are driven by two different mechanisms. The water–ice interface is driven by phase change and the speed of the interface is proportional to the difference between heat flux from the adjacent compartments (which is the classical *Stefan condition* [6]). On the other hand, the gas–water interface moves in response to changes in volume arising from the dissolution of gas in water, as well as volume change owing to the density difference between water and ice.

We next list a number of simplifying assumptions:

(A1) The lateral surface of the cylindrical domain is thermally insulated so that heat flows only in the axial ($x$) direction.

(A2) The system is closed so that the total mass of gas (free plus dissolved) is constant. The total mass of liquid and frozen water also remains constant, although the mass of individual phases may vary.

(A3) Water and ice densities are constant and are not affected by changes in temperature.

(A4) Diffusion in the gas compartment is fast enough in relation to other processes that the gas density can be taken as a function of time only. Indeed, considering the self-diffusion coefficient for air ($D = 2 \times 10^{-5}$ m$^2$/s) and typical length scale ($d = 100$ μm), the time scale for air diffusion is roughly $t \approx d^2/4D = 1.25 \times 10^{-4}$ s (see [5, Section 3.32]).

(A5) The amount of gas that dissolves in the water compartment is small enough relative to the initial gas volume that gas dissolution does not significantly affect the motion of the gas–water interface. When combined with the previous assumption, this implies that the motion of the gas–water interface is due only to the melting of ice and the subsequent density increase as ice changes phase from solid to liquid.

(A6) Neither gas nor water dissolve in or otherwise penetrate the ice layer.

(A7) Some water is always present in the fibre. Instead of having initial conditions where all water is in the frozen state, a very thin layer of liquid is assumed to separate the gas from the ice.

We note that many features of this problem are similar to the sap exudation model derived in [3] for a closed system that consists of two distinct classes of xylem cells: libriform fibres, in which thawing of ice allows compressed gas to force the melted sap through the porous fibre wall; and the neighbouring vessels that contain gas and liquid sap, where the sap in turn contains both dissolved gas and sucrose. This sap exudation model differs from the model that we develop here in several respects:

- We treat only a single compartment containing three phases.

- In [3], the ice in the fibre is sandwiched between the gas and liquid compartments.

- We do not consider osmotic effects or sap flow through the permeable fibre/vessel boundary.

- The simple cylindrical geometry permits us to neglect surface tension effects due to curvature of the gas–water interface.

In the next three sections, we derive the governing equations and boundary conditions in each of the gas, liquid and ice compartments. Following that, we summarise in a separate section the remaining interfacial matching conditions that connect solutions on either side of the moving boundaries.

## 2.1 Gas compartment

Denote the temperature in the gas compartment by $T_g(x,t)$ (°K) which obeys the diffusion equation

$$\rho_g c_g \frac{\partial T_g}{\partial t} = \frac{\partial}{\partial x}\left(k_g \frac{\partial T_g}{\partial x}\right), \tag{2.1a}$$

for $0 < x < s_{gw}(t)$ and $t > 0$. The parameters appearing in this equation are the thermal conductivity $k_g$ (W/m°K) and specific heat $c_g$ (J/kg°K), while the gas density $\rho_g$ (kg/m$^3$) depends on time according to assumption A4. The initial temperature is given by

$$T_g(x,0) = T_{g0}(x), \tag{2.1b}$$

for $0 < x < s_{gw}(0)$. The heat source that drives the melting of the ice compartment is located at the left-hand boundary $x = 0$ where we impose a constant temperature

$$T_g(0,t) = T_1 > T_c, \tag{2.1c}$$

which is strictly greater than the melting temperature of ice, $T_c = 273.15$°K.

Returning to the gas density, we apply assumptions A2 and A4 to derive a closed-form expression for $\rho_g(t)$ using a mass balance argument that considers the total mass of gas (which must be constant) and its division between gas and water compartments. First, the mass (kg) of the dissolved gas in the water compartment is

$$m_w(t) = A M_g \int_{s_{gw}(t)}^{s_{wi}(t)} C(x,t)\,dx, \tag{2.2}$$

where $M_g$ is the molar mass of air (kg/mol), $A = \pi r^2$ is the cross-sectional area of the cylinder (m$^2$) and $C(x,t)$ is the concentration of dissolved gas (mol/m$^3$) (whose governing equation will be given in the next section). The air density may then be written as

$$\rho_g(t) = \frac{A\rho_g(0)s_{gw}(0) - m_w(t) + m_w(0)}{As_{gw}(t)}, \tag{2.3}$$

which along with (2.2) determines $\rho_g(t)$ once the dissolved gas concentration and gas–water/water–ice interface positions are known.

## 2.2 Water compartment

We next turn to the water compartment where the temperature $T_w(x,t)$ satisfies the heat equation

$$\rho_w c_w \left(\frac{\partial T_w}{\partial t} + v \frac{\partial T_w}{\partial x}\right) = \frac{\partial}{\partial x}\left(k_w \frac{\partial T_w}{\partial x}\right), \tag{2.4a}$$

for $s_{gw}(t) < x < s_{wi}(t)$ and $t > 0$, where $c_w$, $\rho_w$ and $k_w$ are the water specific heat, density and thermal conductivity respectively. The extra heat convection term on the left-hand side arises from the slow flow of water due to the melting ice and the

density difference between water and ice [6, 24, 27]; the convection velocity $v$ (m/s) will be specified later in Section 2.4. We also need to specify an initial temperature distribution

$$T_w(x,0) = T_{w0}(x). \tag{2.4b}$$

The dissolved gas concentration $C(x,t)$ obeys the diffusion equation

$$\frac{\partial C}{\partial t} = \frac{\partial}{\partial x}\left(D_w \frac{\partial C}{\partial x}\right), \tag{2.5a}$$

where $D_w$ is the diffusion coefficient for air in water (m$^2$/s). At the gas–water interface, we impose Henry's law

$$C(s_{gw}(t),t) = \frac{H}{M_g}\rho_g(t), \tag{2.5b}$$

which states that the concentration of gas dissolved at the interface is proportional to the density of the gas in contact with the liquid. Here $H$ denotes the dimensionless Henry's constant. Finally, we impose the initial condition

$$C(x,0) = C_0(x), \tag{2.5c}$$

and a no-flux boundary condition at the water–ice interface

$$\frac{\partial C}{\partial x}(s_{wi}(t),t) = 0, \tag{2.5d}$$

which is simply a statement that dissolved gas does not penetrate the ice (in accordance with assumption A6).

The following two remarks relate to the distribution of air between the gaseous and dissolved phases.

**Remark 1** (Conservation of air) *We first show that equation* (2.3) *implies conservation of mass for air in the gaseous and dissolved phases. The total mass of air at any time t can be written as the sum of the air in the water and gas compartments:*

$$m = m_w(t) + A\int_0^{s_{gw}(t)} \rho_g(t)\,dx,$$
$$= m_w(t) + As_{gw}(t)\rho_g(t).$$

*Then replacing $\rho_g(t)$ with* (2.3) *leads to*

$$m = m_w(0) + A\rho_g(0)s_{gw}(0).$$

*This last expression is simply the total initial mass of dissolved and gaseous air, and hence the mass* m *of air is conserved.*

**Remark 2** (Connection with Keller's analysis of gas bubble dynamics) *Our aim here is to derive an expression for the rate of change of the gas density, which can be related directly to an equation derived by Keller for the dynamics of dissolving gas bubbles in water* [16]. *To this end, we take the time derivative of the gas density from equation* (2.3)

$$\frac{d\rho_g}{dt} = \frac{-\dot{m}_w(t)s_{gw}(t) - \dot{s}_{gw}(t)\left[A\rho_g(0)s_{gw}(0) - m_w(t) + m_w(0)\right]}{As_{gw}^2(t)},$$

$$= -\frac{\dot{m}_w(t)}{As_{gw}(t)} - \frac{\rho_g(t)\dot{s}_{gw}(t)}{s_{gw}(t)}, \tag{2.6}$$

*where the 'dot' denotes the time derivative. An expression for* $\dot{m}_w(t)$ *can be obtained by differentiating equation* (2.2)

$$\dot{m}_w(t) = AM_g\left[\dot{s}_{wi}(t)C(s_{wi}(t),t) - \dot{s}_{gw}(t)C(s_{gw}(t),t) + \int_{s_{gw}(t)}^{s_{wi}(t)} \frac{\partial C}{\partial t}(x,t)\,dx\right].$$

*The integral term containing* $\partial_t C$ *can be integrated directly by first replacing* $\partial_t C$ *using the concentration equation* (2.5a)

$$\dot{m}_w(t) = AM_g\left[\dot{s}_{wi}(t)C(s_{wi}(t),t) - \dot{s}_{gw}(t)C(s_{gw}(t),t) + D_w\left(\frac{\partial C}{\partial x}(s_{wi}(t),t) - \frac{\partial C}{\partial x}(s_{gw}(t),t)\right)\right],$$

*and then applying the boundary condition* (2.5d),

$$\dot{m}_w(t) = AM_g\left[\dot{s}_{wi}(t)C(s_{wi}(t),t) - \dot{s}_{gw}(t)C(s_{gw}(t),t) - D_w\frac{\partial C}{\partial x}(s_{gw}(t),t)\right].$$

*We may now substitute this last expression into equation* (2.6) *to obtain*

$$\frac{1}{M_g}\frac{d(\rho_g s_{gw})}{dt} = \dot{s}_{gw}C(s_{gw},t) - \dot{s}_{wi}C(s_{wi},t) + D_w\frac{\partial C}{\partial x}(s_{gw},t). \tag{2.7}$$

*This equation coincides with Keller's equation* (2.6) [16], *except for slight differences arising from to the fact that we are working in a cylindrical geometry and our inclusion of the water–ice interface motion in the evolution of the gas density.*

## 2.3 Ice compartment

In the ice compartment, the equation governing ice temperature $T_i(x,t)$ is

$$\rho_i c_i \frac{\partial T_i}{\partial t} = \frac{\partial}{\partial x}\left(k_i\frac{\partial T_i}{\partial x}\right), \tag{2.8a}$$

for $s_{wi}(t) < x < L$ and $t > 0$, where $c_i$, $\rho_i$ and $k_i$ are the specific heat, density and thermal conductivity of ice. The initial temperature distribution is given by

$$T_i(x,0) = T_{i0}(x), \tag{2.8b}$$

and on the right boundary we impose a convective condition of the form

$$-k_i \frac{\partial T_i}{\partial x}(L, t) = \theta(T_i - T_2),$$ (2.8c)

where $\theta$ is a convective heat transfer coefficient (W/m$^2$ °K) and $T_2$ is a given ambient temperature.

### 2.4 Interfacial and matching conditions

We now state the matching conditions at the two phase interfaces. First, we require that both temperature and heat flux are continuous at the gas–water interface,

$$T_g(s_{gw}(t), t) = T_w(s_{gw}(t), t),$$ (2.9)

$$k_g \frac{\partial T_g}{\partial x}(s_{gw}(t), t) = k_w \frac{\partial T_w}{\partial x}(s_{gw}(t), t).$$ (2.10)

Based on geometric and conservation arguments, we can derive an equation for the evolution of the gas–water interface,

$$\dot{s}_{gw}(t) = \left(1 - \frac{\rho_i}{\rho_w}\right) \dot{s}_{wi}(t),$$ (2.11)

which relates the velocities of the two interfaces via the difference in volume owing to contraction and expansion of ice (details of the derivation are provided in Appendix A). This condition also appears in Crank's book [6, Equation 1.32] as an expression for the velocity of the liquid phase when a density change is taken into account; therefore, we impose

$$v = \dot{s}_{gw}$$ (2.12)

for the convection speed in equation (2.4a).

At the water–ice interface, the temperature must be continuous,

$$T_w(s_{wi}(t), t) = T_i(s_{wi}(t), t) = T_c,$$ (2.13)

with the added requirement that the temperature on both sides of the interface must equal the melting point. The evolution of the water–ice interface is governed by

$$\lambda \rho_i \dot{s}_{wi} = k_i \frac{\partial T_i}{\partial x} - k_w \frac{\partial T_w}{\partial x} \qquad \text{at } x = s_{wi}(t),$$ (2.14)

where $\lambda$ is the latent heat of melting per unit mass (J/kg). This Stefan condition is a statement of conservation of energy, wherein the heat energy generated by phase change ($\lambda \rho_i \dot{s}_{wi}$) is balanced by the difference in heat flux from either side of the phase interface. Finally, to close the system we require initial conditions for the phase interface locations:

$$s_{gw}(0) = s_{gw0},$$ (2.15)

$$s_{wi}(0) = s_{wi0}.$$ (2.16)

Table 1. *Physical parameters, with numerical values taken from* [3]

| Parameter | Symbol | Units | Value |
|---|---|---|---|
| Domain length | $L$ | m | $1.0 \times 10^{-3}$ |
| Domain radius | $r$ | m | $3.5 \times 10^{-6}$ |
| Cross-sectional area | $A = \pi r^2$ | m$^2$ | $3.85 \times 10^{-11}$ |
| Densities | $\bar{\rho}_g$ | kg/m$^3$ | 1.29 |
| | $\rho_w$ | kg/m$^3$ | 1,000 |
| | $\rho_i$ | kg/m$^3$ | 916 |
| Specific heat | $c_g$ | J/kg °K | 1,005 |
| | $c_w$ | J/kg °K | 4,180 |
| | $c_i$ | J/kg °K | 2,050 |
| Thermal conductivities | $k_g$ | W/m °K | 0.0243 |
| | $k_w$ | W/m °K | 0.58 |
| | $k_i$ | W/m °K | 2.22 |
| Thermal diffusivities, $\alpha = k/(\rho c)$ | $\alpha_g$ | m$^2$/s | $1.87 \times 10^{-5}$ |
| | $\alpha_w$ | m$^2$/s | $1.39 \times 10^{-7}$ |
| | $\alpha_i$ | m$^2$/s | $1.18 \times 10^{-6}$ |
| Diffusivity of dissolved air in water | $D_w$ | m$^2$/s | $2.22 \times 10^{-9}$ |
| Molar mass of air | $M_g$ | kg/mol | 0.0290 |
| Henry's constant | $H$ | | 0.0274 |
| Convective heat transfer coefficient | $\theta$ | W/m$^2$ °K | 10.0 |
| Latent heat of melting | $\lambda$ | J/kg | $3.34 \times 10^5$ |
| Critical (melting) temperature of ice | $T_c$ | °K | 273.15 |
| Left boundary temperature | $T_1$ | °K | $T_c + 0.005$ |
| Right boundary temperature | $T_2$ | °K | |

## 2.5 Parameter values

The values of all parameters introduced above are listed in Table 1 in SI units and are taken from the data for the sap exudation model in [3]. The geometrical parameters $L = 10^{-3}$ m, $r = 3.5 \times 10^{-6}$ m and $A = \pi r^2 = 3.85 \times 10^{-11}$ m$^2$ are based on the size of a typical libriform fibre in the xylem of a maple tree.

## 2.6 Non-dimensional equations

Next, we non-dimensionalise the governing equations by introducing the following dimensionless quantities denoted by a superscript asterisk ($^*$):

$$
\begin{aligned}
x &= Lx^*, & s_{gw} &= Ls_{gw}^*, & s_{wi} &= Ls_{wi}^*, \\
t &= \bar{t}t^*, & C &= \bar{C}C^*, & \rho_g &= \bar{\rho}_g\rho_g^*, \\
T_\ell &= T_c + (T_1 - T_c)T_\ell^*. & & & &
\end{aligned}
\tag{2.17}
$$

We choose as a length scale $L = 10^{-3}$ m, which corresponds to a typical length of a libriform fibre [3]. Density is rescaled by the value $\bar{\rho}_g = 1.29$ kg/m$^3$ for air at 1 atm and 0°C, and the concentration by $\bar{C} = \bar{\rho}_g/M_g$. The time scale $\bar{t}$ is chosen equal to the

Table 2. *Characteristic scales and dimensionless parameters*

| Parameter | Expression | Units | Value |
|---|---|---|---|
| $\bar{\rho}_g$ | | kg/m$^3$ | 1.29 |
| $\bar{C}$ | $\dfrac{\bar{\rho}_g}{M_g}$ | mol/m$^3$ | 44.6 |
| $t_w$ | $\dfrac{L^2}{\alpha_w}$ | s | 7.21 |
| $t_i$ | $\dfrac{L^2}{\alpha_i}$ | s | 0.846 |
| $t_g$ | $\dfrac{L^2}{\alpha_g}$ | s | 0.0535 |
| $\bar{t}$ | $\dfrac{L^2 \lambda \rho_i}{k_w(T_1 - T_c)} = \dfrac{t_w \delta}{\mathrm{St}}$ | s | $1.06 \times 10^5$ |
| $\delta$ | $\dfrac{\rho_i}{\rho_w}$ | | 0.916 |
| $\eta$ | $\dfrac{k_w}{k_g}$ | | 23.9 |
| $\psi$ | $\dfrac{k_i}{k_w}$ | | 3.83 |
| Bi | $\dfrac{L\theta}{k_i}$ | | $4.50 \times 10^{-3}$ |
| Le | $\dfrac{\alpha_w}{D_w}$ | | 62.5 |
| St | $\dfrac{(T_1 - T_c)c_w}{\lambda}$ | | $6.26 \times 10^{-5}$ |
| $\widetilde{T}_2$ | $\dfrac{T_2 - T_c}{T_1 - T_c}$ | | |
| $\beta_w$ | $\dfrac{\alpha_w \bar{t}}{L^2} = \dfrac{\delta}{\mathrm{St}}$ | | $1.46 \times 10^4$ |
| $\beta_i$ | $\dfrac{\alpha_i \bar{t}}{L^2} = \dfrac{\alpha_i \beta_w}{\alpha_w}$ | | $1.25 \times 10^5$ |
| $\beta_g$ | $\dfrac{\alpha_g \bar{t}}{L^2} = \dfrac{\alpha_g \beta_w}{\alpha_w}$ | | $1.97 \times 10^6$ |

characteristic scale typical in the Stefan problems for motion of the water–ice interface,

$$\bar{t} = \frac{L^2 \lambda \rho_i}{k_w(T_1 - T_c)}, \tag{2.18}$$

since the melting process is the driving mechanism for this problem.

Substituting the expressions from (2.17) into the model equations and dropping asterisks to simplify notation, we obtain the following dimensionless system where all new parameters are listed in Table 2.

In the gas compartment, $0 < x < s_{gw}(t)$:

$$\rho_g(t)\frac{\partial T_g}{\partial t} = \beta_g \frac{\partial^2 T_g}{\partial x^2}, \tag{2.19a}$$

$$T_g(x,0) = T_{g0}(x) \quad \text{for } 0 < x < s_{gw}(0), \tag{2.19b}$$

$$T_g(0,t) = 1, \tag{2.19c}$$

where the dimensionless diffusion coefficient, $\beta_g = \alpha_g \bar{t}/L^2$, and $\alpha_g = k_g/(\bar{\rho}_g c_g)$ is the thermal diffusivity of air.

In the water compartment, $s_{gw}(t) < x < s_{wi}(t)$, we have equations for both temperature and concentration,

$$\frac{\partial T_w}{\partial t} + \dot{s}_{gw}\frac{\partial T_w}{\partial x} = \beta_w \frac{\partial^2 T_w}{\partial x^2}, \tag{2.20a}$$

$$T_w(x,0) = T_{w0}(x) \quad \text{for } s_{gw}(0) < x < s_{wi}(0), \tag{2.20b}$$

$$\frac{\partial C}{\partial t} = \frac{\delta}{\text{St Le}} \frac{\partial^2 C}{\partial x^2}, \tag{2.21a}$$

$$C(x,0) = C_0(x) \quad \text{for } s_{gw}(0) < x < s_{wi}(0), \tag{2.21b}$$

$$C(s_{gw}(t),t) = H\rho_g(t), \tag{2.21c}$$

$$\frac{\partial C}{\partial x}(s_{wi}(t),t) = 0. \tag{2.21d}$$

Here $\beta_w = \alpha_w \bar{t}/L^2$, $\text{St} = c_w(T_1 - T_c)/\lambda$ is the Stefan number, and the Lewis number $\text{Le} = \alpha_w/D_w$ is a dimensionless ratio of thermal diffusivity of water to the diffusivity of dissolved gas.

In the ice compartment, $s_{wi}(t) < x < 1$:

$$\frac{\partial T_i}{\partial t} = \beta_i \frac{\partial^2 T_i}{\partial x^2}, \tag{2.22a}$$

$$T_i(x,0) = T_{i0}(x) \quad \text{for } s_{wi}(0) < x < 1, \tag{2.22b}$$

$$-\frac{\partial T_i}{\partial x}(1,t) = \text{Bi}(T_i(1,t) - \widetilde{T}_2), \tag{2.22c}$$

where $\beta_i = \alpha_i \bar{t}/L^2$ and $\widetilde{T}_2 = (T_2 - T_c)/(T_1 - T_c)$. The Biot number $\text{Bi} = L\theta/k_i$ is a measure of the relative resistance to heat transfer of the outer surface of the ice to that in the interior.

The non-dimensional forms of the interfacial conditions at the gas–water interface are

$$\frac{\partial T_g}{\partial x}(s_{gw}(t), t) = \eta \frac{\partial T_w}{\partial x}(s_{gw}(t), t), \tag{2.23}$$

$$T_g(s_{gw}(t), t) = T_w(s_{gw}(t), t), \tag{2.24}$$

while at the water–ice interface

$$T_w(s_{wi}(t), t) = T_i(s_{wi}(t), t) = 0. \tag{2.25}$$

Equation (2.3) for the gas density reduces to

$$\rho_g(t) = \frac{s_{gw}(0) + \int_{s_{gw}(0)}^{s_{wi}(0)} C_0(x)\, dx - \int_{s_{gw}(t)}^{s_{wi}(t)} C(x, t)\, dx}{s_{gw}(t)}. \tag{2.26}$$

The gas–water interface equation (2.11) becomes

$$\dot{s}_{gw}(t) = (1 - \delta)\, \dot{s}_{wi},$$

where $\delta = \rho_i / \rho_w$, which can be integrated directly to obtain

$$\left. \begin{array}{l} s_{gw}(t) = A_1 + A_2 s_{wi}(t) \\ \text{where} \quad A_1 = s_{gw}(0) - (1 - \delta)\, s_{wi}(0) \\ \text{and} \quad A_2 = 1 - \delta \end{array} \right\}. \tag{2.27}$$

Finally, the dimensionless form of the Stefan condition (2.14) is

$$\dot{s}_{wi} = \left( \psi \frac{\partial T_i}{\partial x}(s_{wi}, t) - \frac{\partial T_w}{\partial x}(s_{wi}, t) \right), \tag{2.28}$$

where $\psi = k_i / k_w$. Note that the time scale $\bar{t}$ in (2.18) was chosen so that the coefficient in front of $\dot{s}_{wi}$ scales to one. Comparing $\bar{t}$ with the corresponding time scales for heat diffusion ($t_g$, $t_w$ and $t_i$ in Table 2), it is clear that the front motion occurs over a much slower time scale.

In summary, our model consists of a coupled nonlinear system of equations that comprises the following:

- Four partial differential equation (PDE) initial-boundary value problems (2.19)–(2.22) for the temperatures and dissolved gas concentration.
- One ordinary differential equation (ODE) initial value problem (2.28) for the water–ice interface position.
- Two algebraic equations (2.26) and (2.27) for gas density and gas–water interface position.

Because of the nonlinearity in the equations, we have been unable to derive an analytical solution and so we resort to numerical simulations or approximate analytic methods. In the next section, we describe our solution algorithm and present numerical simulations that in turn suggest an appropriate form for an approximate analytical solution.

## 3 Numerical solution algorithm

We begin by describing our approach for solving the PDEs governing temperature and concentration. We use the method of lines, discretising first in space using a cell-centred grid and then solving the resulting system of time-dependent ODEs. To capture moving boundaries sharply, we employ a moving mesh approach in which $N$ equally spaced grid points are distributed over each of the gas, water and ice domains so that

$$x_g^j(t) = (j - 1/2)h_g(t) \qquad \text{with } h_g(t) = \frac{s_{gw}(t)}{N},$$

$$x_w^j(t) = s_{gw}(t) + (j - 1/2)h_w(t) \qquad \text{with } h_w(t) = \frac{s_{wi}(t) - s_{gw}(t)}{N},$$

$$x_i^j(t) = s_{wi}(t) + (j - 1/2)h_i(t) \qquad \text{with } h_i(t) = \frac{1 - s_{wi}(t)}{N},$$

for $j = 1, 2, \ldots, N$, and where $h_\ell(t)$ for $\ell = g, w, i$ denotes the grid spacing on the corresponding compartment. When using such a moving grid, we must introduce an additional convection term in each parabolic PDE owing to the grid motion [12, 14]

$$\frac{\partial f}{\partial t} - u \frac{\partial f}{\partial x} = \kappa \frac{\partial^2 f}{\partial x^2}, \tag{3.1}$$

where $f = T_g, T_w, T_i, C$ and $\kappa = \beta_g, \beta_w, \beta_i, \delta/(\mathrm{St}\,\mathrm{Le})$ respectively. The convective term has a velocity $u$ equal to the mesh velocity $\dot{x}_\ell$ in the gas and ice compartments, but equal to $\dot{x}_w - \dot{s}_{gw}$ in the water compartment because of the presence of additional convective term in equation (2.20a).

Our numerical approach is similar in spirit to the coordinate transformation method described by Furzeland [12] and the boundary immobilization method employed by Mitchell and Vynnycky [21]. There are also many other possible numerical approaches, including the enthalpy method, finite element method and heat balance integral method, which are discussed in [12, 21] and the references therein.

The spatial derivatives appearing in equation (3.1) are replaced using centred, second-order difference approximations to obtain

$$\frac{\partial f_\ell^j}{\partial t} - u_\ell^j \frac{f_\ell^{j+1} - f_\ell^{j-1}}{2h_\ell} = \kappa_\ell \frac{f_\ell^{j+1} - 2f_\ell^j + f_\ell^{j-1}}{h_\ell^2}, \tag{3.2}$$

where $f_\ell^j(t) \approx f(x_\ell^j, t)$ are the discrete approximations of the dependent variables for $\ell = g, w, i$ and $j = 1, 2, \ldots, N$. Centred finite differences are also used to discretise the boundary conditions and hence maintain second-order accuracy throughout. This requires values of the approximate solution that lie within a grid cell lying immediately outside of each compartment; to this end we introduce fictitious points $x_\ell^0 = x_\ell^1 - h_\ell$ and $x_\ell^{N+1} = x_\ell^N + h_\ell$. A Dirichlet boundary condition such as (2.19c) is approximated using an arithmetic average

$$\frac{T_g^0 + T_g^1}{2} = 1,$$

which is solved for the fictitious value as $T_g^0 = 2 - T_g^1$. Furthermore, a Neumann boundary

condition such as (2.22c) is approximated by

$$-\frac{T_i^{N+1} - T_i^N}{h_i} = \text{Bi}\left(\frac{T_i^N + T_i^{N+1}}{2} - \widetilde{T}_2\right),$$

which yields

$$T_i^{N+1} = \frac{(2 - h_i\,\text{Bi})\,T_i^N + 2h_i\,\text{Bi}\,\widetilde{T}_2}{2 + h_i\,\text{Bi}}.$$

The remaining fictitious point values are obtained in a similar manner for the other boundary and matching conditions. Finally, integrals of concentration that appear in the boundary condition (2.21c) (via the density (2.26)) are approximated using the trapezoidal rule so that the resulting spatial discretisation is fully of second order in space.

The semi-discrete temperature and concentration equations comprise a system of $4N$ time-dependent ODEs. One additional ODE is derived from the water–ice interface equation (2.28) in which the spatial derivatives are also approximated using centred differences. The resulting system of $4N + 1$ ODEs is implemented in the Matlab® programming environment and integrated in time using the stiff solver ode15s. In all the cases, the error tolerances for ode15s are set to AbsTol=1e-10 and RelTol=1e-8.

To validate the order of accuracy of our results, we performed a convergence study using parameters from the 'base case' described in the next section and for grids with $N$=10, 20, 40  and  80. We take the two-norm difference of temperature solutions on successive grids as a measure of the solution error, which we compute using

$$E_N = \left\{\frac{1}{N}\sum_{\ell=1}^{N}\left(T_\ell[N] - T_{2\ell}[2N]\right)^2\right\}^{1/2}.$$

The error values $E_N$ are plotted versus $N$ in Figure 2, which clearly demonstrates that our numerical solution converges as the spatial grid is refined. Furthermore, the points are well represented on a log–log scale by the least-squares linear fit with a slope of roughly 2.132. This suggests that our numerical method also converges with the expected second-order spatial accuracy.

## 4 Numerical simulations

We now employ the method described in the previous section to simulate the model equations and to evaluate sensitivity to various physical parameters. In all simulations, we take $N$=100 grid points for each compartment and also make the following choices for initial conditions:

- $s_{gw}(0) = 0.1$ and $s_{wi}(0) = 0.11$ so that the water is initially completely frozen except for a thin liquid layer (refer to assumption A7).
- $C(x,0) \equiv 0$, corresponding to no dissolved gas.
- $T_g(x,0) \equiv T_w(x,0) \equiv 1$ and $T_i(x,0) \equiv \widetilde{T}_2$ so that the gas and water compartments
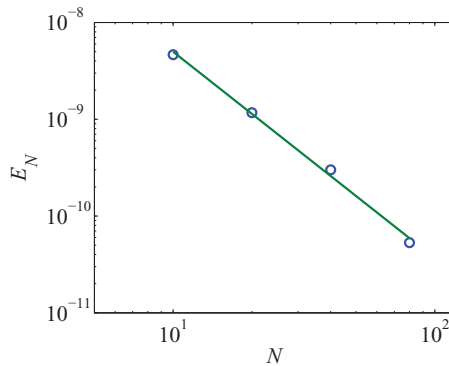
FIGURE 2. (Colour online) Convergence study for the numerical solution with grids of size $N=10$, 20, 40, 80. The points represent the $\ell_2$-norm difference between computed temperatures on successive grids, and the solid line denotes a linear least squares fit to the points.

are equilibrated with the left boundary temperature, while the ice compartment is equilibrated with the ambient (sub-freezing) temperature at the right boundary.

We begin by focusing on the water–ice front motion that drives the phase change dynamics and in turn influences gas dissolution. We consider as a 'base case' the situation where the boundary temperatures are $T_1 = T_c + 0.005$ and $T_2 = T_c - 0.005$, for which results are provided in Figure 3. Two other cases with larger values of $T_1$ and $T_2$ are presented in Figures 4 and 5 for comparison purposes. Note that all plots are shown in dimensionless variables.

In the base case, the plot in Figure 3(a) of the dissolved gas concentration (measured at the right-hand boundary) exhibits a clear division of the solution behaviour into three separate time periods:

(1) A very short initial transient during which the concentration undergoes a rapid increase from zero at $t = 0$ to some maximum value at time $t \sim O(10^{-7})$. This transition layer arises because we have chosen initial conditions corresponding to zero dissolved gas and hence Henry's law forces the initially very thin water layer to rapidly 'fill up' with gas. The corresponding diffusion of dissolved gas within the water compartment can be seen in Figure 3(c).

(2) The gas concentration remains roughly unchanged over the interval $t \in (10^{-7}, 10^{-2})$, since the water does not yet melt appreciably.

(3) The time $t \sim O(10^{-2})$ signals the onset of ice melting, after which the water compartment begins to grow in size. Even though this allows more gas to dissolve in the water layer, the increased volume leads to a decrease in the dissolved gas concentration as the pressure in the gas compartment decreases. This effect is evident in Figure 3(b), where the concentration profiles throughout the water layer are roughly constant in $x$, although there is a slight increase in $C$ from left to right.

The presence of these three clearly separated time scales is a characteristic feature of the evolution of dissolved gas. Because the concentration profiles are almost constant in $x$

(a) Gas concentration at $x = L$.

(b) Gas concentration profiles (long time).

(c) Concentration profiles (short time).

(d) Phase interfaces.

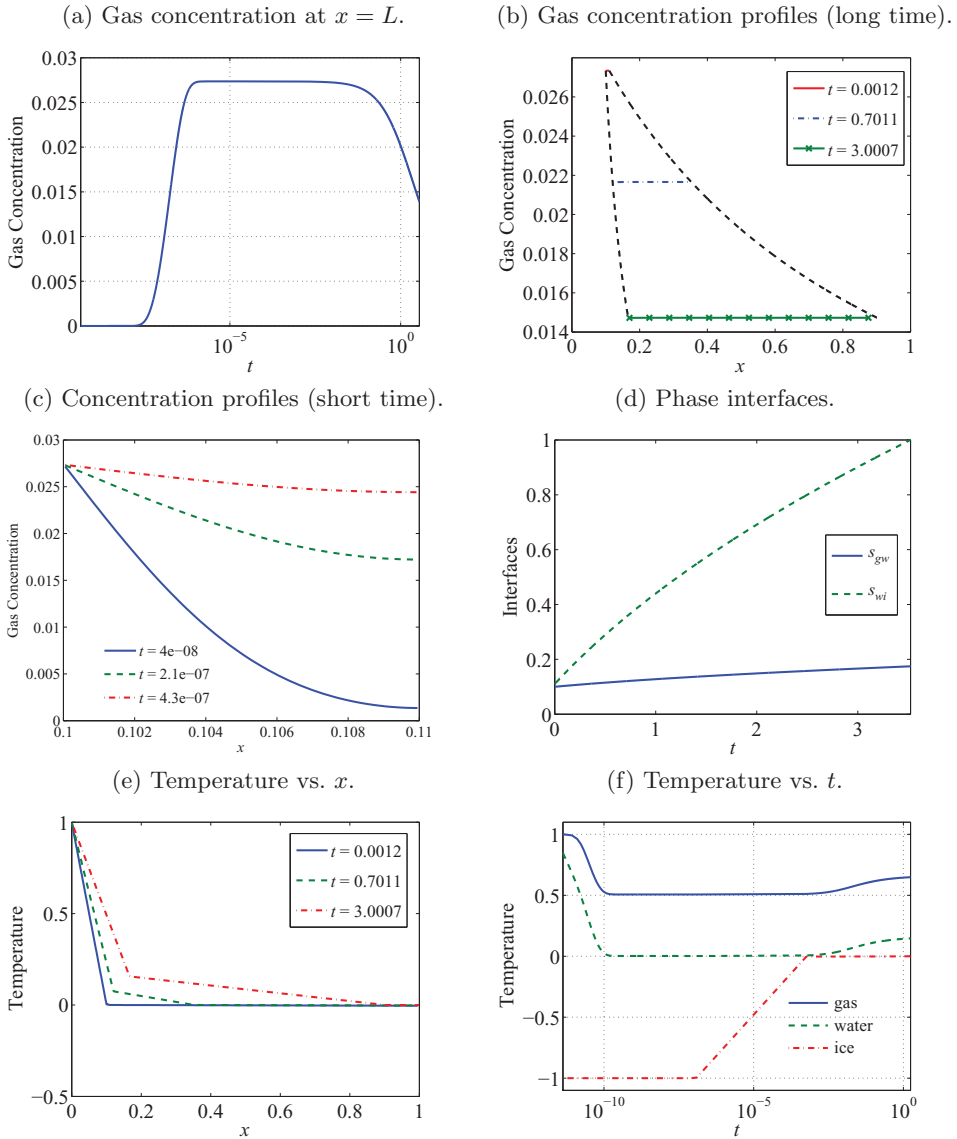(e) Temperature vs. $x$.

(f) Temperature vs. $t$.

FIGURE 3. (Colour online) Solution plots with boundary temperatures $T_1 = T_c + 0.005$ and $T_2 = T_c - 0.005$, with $\tilde{T}_2 = -1$.

over longer times, the gas concentration dynamics are driven primarily by the relative motion of the free boundaries.

A somewhat counter-intuitive observation is that after initial transients are complete, $C$ attains its maximum value at the water–ice interface rather than at the gas–water interface where dissolution is actually taking place. This slight positive slope in the plot of $C$ versus $x$ becomes more pronounced as the boundary temperature difference $T_1 - T_2$ is increased, and can be seen most clearly in Figure 5(b) where the temperature difference is
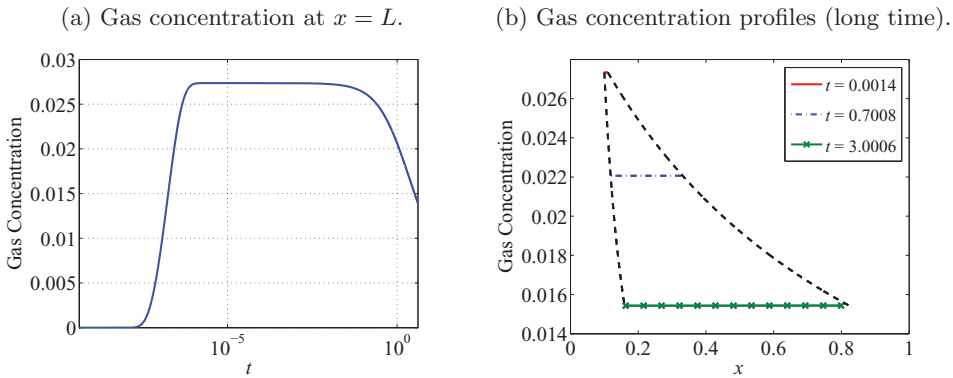
(a) Gas concentration at $x = L$.  (b) Gas concentration profiles (long time).



FIGURE 4. (Colour online) Solution plots with boundary temperatures $T_1 = T_c + 0.005$ and $T_2 = T_c - 0.02$, with $\tilde{T}_2 = -4$.

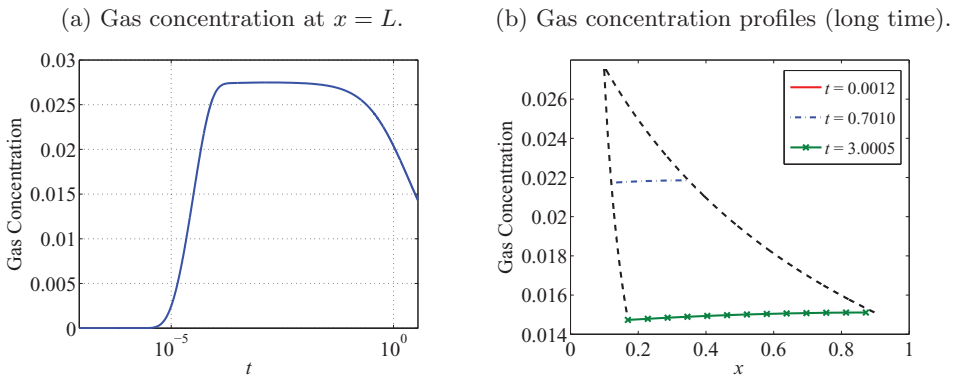(a) Gas concentration at $x = L$.  (b) Gas concentration profiles (long time).



FIGURE 5. (Colour online) Solution plots with boundary temperatures $T_1 = T_c + 1$ and $T_2 = T_c - 1$, $\tilde{T}_2 = -1$.

the largest. We also remark that the speed of the free boundaries increases with $T_1 - T_2$, which allows less time for the gas to adjust in the water compartment.

We close our discussion of the base case with a look at the final two plots in Figure 3. The water–ice interface in Figure 3(d) shows the expected sub-linear behaviour that is consistent with the $t^{1/2}$ dependence predicted by analytical solutions of the Stefan problem. This behaviour is confirmed by our asymptotic results in Section 5.2. The initial transient behaviour of the solution consisting of a rapid adjustment to the initial conditions is depicted in Figure 3(f), which plots the temperature at the mid-point of each compartment versus time. We observe a clear separation of time scales wherein the gas and water compartments equilibrate first, and the ice compartment requires a significantly longer time period. The relative speed of the gas and ice transients is consistent with the discussion of time scales later in Section 5.1; however, time scale predicted for water is much slower than the initial transient observed here because the initial thickness of the water layer is very thin in comparison with the domain length scale $L$. After these initial transients, the temperature solution adjusts much more gradually over longer times as shown in Figure 3(e). Furthermore, we observe that the temperature is continuous and
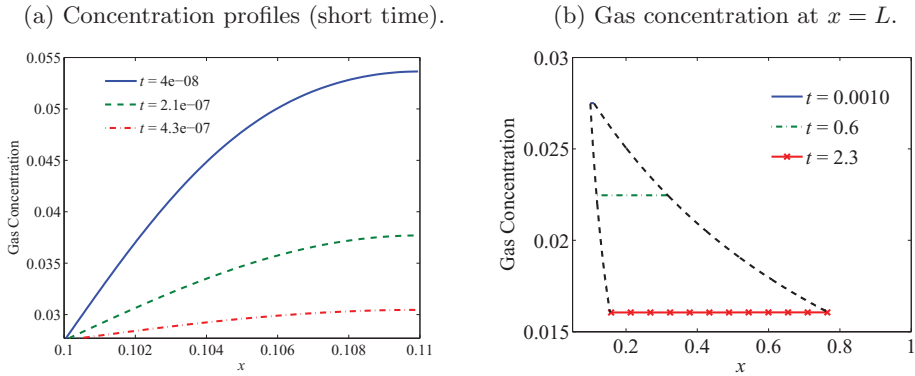
(a) Concentration profiles (short time).          (b) Gas concentration at $x = L$.



FIGURE 6. (Colour online) Solution plots with boundary temperatures $T_1 = T_c + 0.005$, $T_2 = T_c - 0.005$, $\tilde{T}_2 = -1$ and $C_0(y) = 2\bar{C}$.

approximately linear within each compartment, with a pronounced 'kink' at the interface locations. All of these results will be explained by the analytical solution derived in Section 5.

The effect of increasing the temperature difference $T_1 - T_2$ can be seen by comparing the results in Figures 4 and 5 with those in Figure 3. There is a significant slowing of the initial transient gas dissolution dynamics as $T_1 - T_2$ is increased, although the long time concentration dynamics are largely unchanged. However, as mentioned above, there is a slight increase in the slope of concentration profiles in Figure 5(b).

Comparing Figures 3–5, we remark that for the base case with temperature increments of 0.005, the ice layer melts away after about 1 h. In contrast, the melting time shortens to 17 s when the temperature increment is taken as large as 1.0. The only place that $\bar{T}_1$ enters the model is through the Stefan number St, which explains why changes in $\bar{T}_1$ have the effect of altering the time scale for the free boundary motion.

We conclude this section by investigating the effect of taking a large initial value of dissolved gas concentration, $C(x, 0) \equiv 0.055$, rather than taking $C(x, 0) \equiv 0$ as we have so far. We will see later that this initial concentration is large in the sense that it is twice the steady-state value of concentration for the base case; hence, we may view this as a 'super-saturated' case in which one would expect dissolved gas to immediately cavitate and form bubbles. The results in Figure 6(a) are consistent with this hypothesis, and show that the behaviour of the concentration profiles is reversed relative to the base case in Figure 3(c) in that concentration decreases from the initial value to its quasi-steady state.

## 5 Approximate analytical solutions

Motivated by the numerical results in the previous section, we now derive an approximate analytical solution that is based on the following observations:

- The temperature is approximately linear in each compartment, and equilibrates rapidly to changes in conditions over the time scale of the interface motion. This suggests using a quasi-steady approximation for each temperature variable.
- The dissolved gas concentration evolves on two time scales: a rapid initial equilibration

phase driven by diffusion (on the order of $10^{-8}$–$10^{-5}$ s) during which gas dissolves at the gas–water interface to fill the liquid compartment; and a longer melting time scale (on the order of $t = 0.01$–$0.1$ s) when the water–ice interface begins to move and the volume of the water compartment increases appreciably.

As a result, we approximate the solution in three stages. First, we make a quasi-steady approximation for temperature that permits us to write $T_\ell(x,t)$ as linear functions of $x$ for $\ell = g, w, i$ that vary in time only through changes in the interface locations. Second, we derive a simpler ODE for the water–ice interface $s_{wi}(t)$ that employs a series expansion in the small parameter Bi, which then also yields an approximation for $s_{gw}(t)$ via equation (2.27). Finally, we develop a two-layer asymptotic solution for the dissolved gas concentration $C(x,t)$ based on the separation of time scales mentioned above.

### 5.1 Quasi-steady approximation for temperatures

The time scales for diffusion of heat in the gas, water and ice compartments can be estimated using

$$t_\ell = \frac{L^2}{\alpha_\ell} \qquad \text{for } \ell = g, w, i,$$

where the thermal diffusivities $\alpha_\ell$ and the length scale $L$ are taken from Tables 1 and 2. The corresponding time scales are $t_g \approx 0.0535$ s, $t_w \approx 7.21$ s and $t_i \approx 0.846$ s. In contrast, the time scale $\bar{t} \approx 1.06 \times 10^5$ is several order of magnitude higher, and consequently the phase temperatures will adjust rapidly in response to any motion of interfaces. It is therefore reasonable to assume that the temperatures $T_\ell$ are quasi-steady in the sense that they do not depend explicitly on time but instead have an implicit dependence on $t$ through the free boundary locations $s_{gw}(t)$ and $s_{wi}(t)$. Note that small values of $t_w$, $t_i$, $t_g$ are equivalent to large values of the dimensionless heat diffusion coefficients $\beta_w$, $\beta_i$, $\beta_g$, whose actual values in Table 2 range between $O(10^4)$ and $O(10^6)$. Taking the limit as $\beta_\ell \to \infty$ in equations (2.19a), (2.20a) and (2.22a) clearly justifies the use of a quasi-steady approximation for temperatures.

The convective term in the water equation (2.20a) is so small (on the order of $10^{-2}$) that it can be neglected. Therefore, the quasi-steady temperature equation in all compartments is $\partial_{xx} T_\ell = 0$, and consequently the temperature is well approximated by linear functions of $x$:

$$T_\ell(x,t) = a_\ell(t)x + b_\ell(t) \qquad \text{for } \ell = g, w, i. \tag{5.1}$$

Coefficients $a_\ell(t)$ and $b_\ell(t)$ can be determined by imposing boundary and matching conditions (2.19c), (2.22c) and (2.23)–(2.25), after which we obtain

$$T_g(x,t) = -\frac{\eta(x - s_{gw}) + s_{gw} - s_{wi}}{s_{wi} + (\eta - 1)s_{gw}}, \tag{5.2a}$$

$$T_w(x,t) = \frac{s_{wi} - x}{s_{wi} + (\eta - 1)s_{gw}}, \tag{5.2b}$$

$$T_i(x,t) = \frac{\text{Bi } \widetilde{T}_2(x - s_{wi})}{1 + \text{Bi}(1 - s_{wi})}. \tag{5.2c}$$

### 5.2 Asymptotic expansion for water–ice interface

We next derive an analytical solution for the water–ice interface $s_{wi}(t)$ by substituting the approximations just derived for $T_i$ and $T_w$ into the Stefan condition (2.28) along with expression (2.27) for $s_{gw}$ to obtain the following ODE,

$$(B_1 + B_2 s_{wi})(1 + \text{Bi}(1 - s_{wi}))\dot{s}_{wi} = (1 + \text{Bi}(B_5 + B_6 s_{wi})). \tag{5.3}$$

The constants appearing in this equation are

$$\begin{aligned}
B_1 &= (\eta - 1)A_1, & B_2 &= 1 + (\eta - 1)A_2, \\
B_3 &= B_1 s_{wi}(0) + B_2 \frac{s_{wi}^2(0)}{2}, & B_4 &= B_1 s_{wi}(0) + \frac{B_2 - B_1}{2}s_{wi}^2(0) - \frac{B_2}{3}s_{wi}^3(0), \\
B_5 &= 1 + \psi \widetilde{T}_2 B_1, & B_6 &= \psi \widetilde{T}_2 B_2 - 1,
\end{aligned}$$

whereas $A_1$ and $A_2$ are the same constants defined earlier in equation (2.27). This ODE can be integrated over the interval $[0, t]$ to obtain the following integral equation for $s_{wi}$:

$$\begin{aligned}
B_1 s_{wi} &+ \frac{B_2}{2}s_{wi}^2 + \text{Bi}\left[B_1 s_{wi} + \frac{B_2 - B_1}{2}s_{wi}^2 - \frac{B_2}{3}s_{wi}^3\right] \\
&= B_3 + t + \text{Bi } B_4 + \text{Bi}\left[B_5 t + B_6 \int_0^t s_{wi}(l)\,dl\right]. 
\end{aligned} \tag{5.4}$$

Because the Biot number satisfies $\text{Bi} \ll 1$ (see Table 2), it is reasonable to look for a series solution of the form

$$s_{wi}(t) = s_0(t) + \text{Bi } s_1(t) + O(\text{Bi}^2). \tag{5.5a}$$

Substituting this expression into (5.4) and collecting terms in like powers of Bi, we find that to leading order

$$s_0(t) = \frac{1}{B_2}\left(\sqrt{B_1^2 + 2B_2(B_3 + t)} - B_1\right), \tag{5.5b}$$

while the next order correction is

$$\begin{aligned}
s_1(t) = \frac{1}{B_1 + B_2 s_0(t)} &\left(\frac{B_2}{3}s_0(t)^3 + \frac{B_1 - B_2}{2}s_0(t)^2 - B_1 s_0(t) + B_4\right. \\
&\left. + B_5 t + B_6 \int_0^t s_0(l)\,dl\right).
\end{aligned} \tag{5.5c}$$

Using the water–ice interface approximation in equations (5.5) the gas–water interface may be determined from (2.27).

We conclude this section by drawing a connection between the leading order solution $s_0(t)$ in the limit as $\text{Bi} \to 0$ and the classical solution of the Stefan problem where the
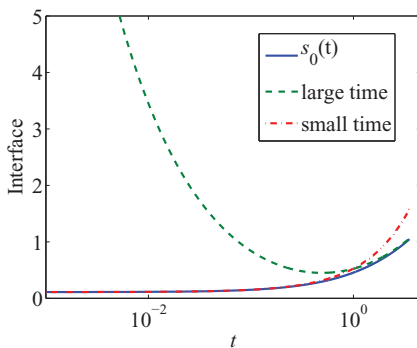
FIGURE 7. (Colour online) Series expansions of $s_0(t)$ for large and small times, showing the expected $\sqrt{t}$ behaviour as $t \to \infty$ (note that the $t$-axis is on a log scale).

melting front moves with a speed proportional to $t^{1/2}$. Although equation (5.5b) does not have exactly this form, the behaviour is consistent in the limits of large and small time. In particular, if we expand (5.5b) in the Taylor series about $t = 0$, we find that

$$s_0(t) = \frac{\sqrt{B_1^2 + 2B_2 B_3} - B_1}{B_2} + \frac{2}{\sqrt{B_1^2 + 2B_2 B_3}} t + O(t^2) \qquad \text{(as } t \to 0\text{).} \qquad (5.6)$$

Furthermore, the large time limit of (5.5b) yields

$$s_0(t) = \frac{-B_1}{B_2} + \left(\frac{2t}{B_2}\right)^{1/2} + \frac{B_1^2 + 2B_2 B_3}{2B_2^2}\left(\frac{2t}{B_2}\right)^{-1/2} + O(t^{-3/2}) \qquad \text{(as } t \to \infty\text{).} \qquad (5.7)$$

When these series expansions are plotted against the exact expression for $s_0(t)$ in Figure 7, we see that both match well for small and large times; in particular, the large time expansion (5.7) shows the expected $t^{1/2}$ behaviour. This leading order behaviour of the phase interface in the quasi-steady regime is common in other phase change problems, for example the diffusion of solvent in glassy polymers [4] or silicon oxidation [7].

### 5.3 Two-scale asymptotic solution for gas concentration

The numerical simulations from Section 4 (see Figures 3(a), 4(a) and 5(a)) exhibited a clear separation of time scales during the evolution of the dissolved gas concentration. Starting from a given initial value, the concentration increases rapidly as gas dissolves at the gas–water interface and diffuses through the water compartment. We recall our earlier observation that the gas concentration is nearly constant in space, with a slight positive slope that leaves the maximum value at the water–ice interface (see Figure 5(b)); this maximum is attained over the short diffusion time scale before the free boundaries begin to move. From then on the dissolved gas concentration remains essentially linear and decreases over a much longer time scale that is driven by the motion of the free boundaries. It is this dual time-scale behaviour that we aim to explain in this section.

To this end, it is helpful to derive rough estimates of the time and length scales

involved. The time required for the dissolved gas to diffuse a distance $d = \frac{L}{2}(s_{wi}(0) - s_{gw}(0))$ corresponding to half the width of the water compartment is

$$t_d = \frac{d^2}{D_w} \approx 1.13 \times 10^{-2} \text{ s.} \tag{5.8}$$

This value should be compared with the time $t_{wi}$ required for the ice to melt completely, which can be estimated by setting $s_{wi}(t_{wi}) = 1$ in equation (5.5) and focusing on the leading order term to obtain

$$t_{wi} = \frac{\bar{t}}{2}(B_2 + 2B_1 - 2B_3) \approx 96.4 \text{ h,}$$

which is six orders of magnitude larger than the diffusion scale $t_d$ in (5.8). Furthemore, on this same time scale the water–ice interface is only capable of travelling a distance of

$$L(s_{wi}(t_d) - s_{wi}(0)) \approx 2.25 \times 10^{-8} \text{L.}$$

Hence, the phase interfaces can be treated as stationary over the diffusive time scale $t_d$.

Based on these observations, we now develop a two-layer asymptotic expansion for the dissolved gas concentration. We begin by rescaling the dimensionless spatial variable as

$$y = \frac{x - s_{gw}(0)}{\Delta s}, \tag{5.9}$$

where $\Delta s = s_{wi}(0) - s_{gw}(0) > 0$. By substituting into equation (2.21a) and defining a new concentration variable $G(y, t) = C(x, t)$, we obtain

$$\frac{\partial G}{\partial t} = \frac{1}{\epsilon} \frac{\partial^2 G}{\partial y^2}, \tag{5.10}$$

where the new diffusion parameter is

$$\epsilon = \frac{\text{Le St}}{\delta}(\Delta s)^2 \ll 1.$$

It is convenient at this point to rescale interface positions according to

$$\sigma_{wi}(t) = \frac{s_{wi}(t) - s_{gw}(0)}{\Delta s} \qquad \text{and} \qquad \sigma_{gw}(t) = \frac{s_{gw}(t) - s_{gw}(0)}{\Delta s}.$$

Two series expansions will next be developed for the concentration variable $G(y, t)$: one for long times corresponding to $t = O(1)$, and the second for shorter times corresponding to $t = O(\epsilon) \ll 1$. A similar solution structure is seen in the study of silicon oxidation by King [17], although our analysis is distinguished from his by the appearance of non-orthogonal eigenfunctions in series expansions.

5.3.1 *Large time expansion, $t = O(1)$*

For large times, we suppose that the dissolved gas concentration is a series in the small parameter $\epsilon$:

$$G(y,t) = G_0(y,t) + \epsilon G_1(y,t) + O(\epsilon^2). \tag{5.11}$$

Substituting this expression into (5.10) and collecting terms with like powers of $\epsilon$ gives rise to the leading order equation

$$\frac{\partial^2 G_0}{\partial y^2} = 0,$$

which has solution $G(y,t) = a(t)y + b(t)$, similar to the quasi-steady approximation for temperature that we obtained in Section 5.1. The leading order boundary conditions corresponding to (2.21c) and (2.21d) are

$$\frac{\partial G_0}{\partial y}(\sigma_{wi}(t), t) = 0,$$

$$G_0(\sigma_{gw}(t), t) = \frac{H\zeta + H\left(\int_0^1 C_0(y)\,dy - \int_{\sigma_{gw}(t)}^{\sigma_{wi}(t)} G_0(y,t)\,dy\right)}{\zeta + \sigma_{gw}(t)},$$

where we have introduced the notation

$$\zeta = \frac{s_{gw}(0)}{\Delta s}, \tag{5.12}$$

which is a positive constant because $\Delta s > 0$ by assumption A7. The zero Neumann boundary condition requires that $a(t) \equiv 0$ and hence the leading order solution is

$$G_0(y,t) = \frac{H\zeta + H\int_0^1 C_0(y)\,dy}{\zeta + \sigma_{gw} + H(\sigma_{wi} - \sigma_{gw})}. \tag{5.13}$$

At the next order in $\epsilon$, we obtain the following boundary value problem for $G_1(y,t)$

$$\frac{\partial^2 G_1}{\partial y^2} = \frac{\partial G_0}{\partial t},$$

$$\frac{\partial G_1}{\partial y}(\sigma_{wi}(t), t) = 0,$$

$$G_1(\sigma_{gw}(t), t) = -H\xi(t)\int_{\sigma_{gw}(t)}^{\sigma_{wi}(t)} G_1(y,t)\,dy,$$

where we have defined

$$\xi(t) = \frac{1}{\zeta + \sigma_{gw}(t)}. \tag{5.14}$$

Using a similar argument to the leading order solution, we obtain

$$
G_1(y,t) = \frac{\partial G_0}{\partial t}(y,t) \left[ \frac{y^2}{2} - \sigma_{wi}y - \frac{\frac{\sigma_{gw}^2}{2} - \sigma_{wi}\sigma_{gw} + \xi \left( \frac{\sigma_{wi}^3 - \sigma_{gw}^3}{6} - \frac{\sigma_{wi}^2 - \sigma_{gw}^2}{2} \right)}{1 + \xi(\sigma_{wi} - \sigma_{gw})} \right]. \qquad (5.15)
$$

Note that $\partial_t G_0 < 0$ so that $G_1$ is an increasing and concave downward function of $y$ that attains its maximum value at the right-hand endpoint $y = \sigma_{wi}$; therefore, the asymptotic solution exhibits the same behaviour observed earlier in the numerical results for concentration in Figure 5(b).

### 5.3.2 *Short time expansion, $t = O(\epsilon)$*

For much shorter times with $t = O(\epsilon)$, we rescale the time variable according to

$$
\tau = \frac{t}{\epsilon}, \qquad (5.16)
$$

and also denote the short-time expansion for concentration by $\gamma(y, \tau) = C(x, t)$, where $y$ is the same rescaled spatial variable in (5.9). Under this scaling the concentration diffusion equation (5.10) reduces to

$$
\frac{\partial \gamma}{\partial \tau} = \frac{\partial^2 \gamma}{\partial y^2}. \qquad (5.17)
$$

As mentioned before, over such a short time interval the interfaces are essentially stationary and so we seek a solution $\gamma$ on a fixed interval $y \in [\sigma_{gw}(0), \sigma_{wi}(0)] = [0, 1]$. The initial and boundary conditions (2.21b)–(2.21d) may then be written in terms of $\gamma$ as

$$
\gamma(y, 0) = C_0(y),
$$
$$
\gamma(0, \tau) = H + \frac{H}{\zeta} \left( \int_0^1 C_0(y)\, dy - \int_0^1 \gamma(y, \tau)\, dy \right),
$$
$$
\frac{\partial \gamma}{\partial y}(1, \tau) = 0.
$$

We begin by determining the steady state solution for this problem, which is simply a constant value

$$
\gamma_\infty = \frac{H\zeta + H \displaystyle\int_0^1 C_0(y)\, dy}{\zeta + H}.
$$

We then define $\hat{\gamma}(y, \tau) = \gamma(y, \tau) - \gamma_\infty$, which satisfies the same equation (5.17) along with

the following modified initial and boundary conditions,

$$\hat{\gamma}(y, 0) = C_0(y) - \gamma_{\infty},$$

$$\hat{\gamma}(0, \tau) = -\frac{H}{\zeta} \int_0^1 \hat{\gamma}(y, \tau) \, dy,$$

$$\frac{\partial \hat{\gamma}}{\partial y}(1, \tau) = 0.$$

This modified problem can be solved by the method of separation of variables to obtain

$$\hat{\gamma}(y, \tau) = \sum_{n=1}^{\infty} a_n \cos\left(\mu_n(y - 1)\right) e^{-\mu_n^2 \tau}, \tag{5.18}$$

where $\mu_n$ are solutions to the nonlinear equation

$$\mu_n \zeta + H \tan \mu_n = 0. \tag{5.19}$$

In the method of separation of variables, it is customary to determine the series coefficients $a_n$ by multiplying the initial condition

$$C_0(y) - \gamma_{\infty} = \sum_{n=1}^{\infty} a_n \cos\left(\mu_n(y - 1)\right)$$

by another eigenfunction from the set $\mathscr{F} = \{\cos(\mu_n(y - 1)) \mid n = 1, 2, \dots\}$, then integrating and applying an orthogonality relation to simplify the result. We note that $\mathscr{F}$ is an orthonormal set of eigenfunctions for the diffusion problem with mixed (Dirichlet/Neumann) and *homogeneous* boundary conditions, where the eigenvalues are $\mu_n = (2n - 1)\frac{\pi}{2}$. In contrast, the eigenfunctions in the problem at hand are not orthogonal because of the integral boundary condition at $y = 0$ that leads to a more complicated eigenvalue equation (5.19), for which $\mu_n$ only approaches $(2n - 1)\frac{\pi}{2}$ as $n \to \infty$. As a result, the eigenfunctions satisfy

$$\int_0^1 \cos(\mu_n(y - 1)) \cos(\mu_\ell(y - 1)) \, dy = \begin{cases} \frac{1}{2} + \frac{\zeta}{2} \cos^2(\mu_n), & \text{if } n = \ell, \\ \zeta \cos(\mu_n) \cos(\mu_\ell), & \text{if } n \neq \ell. \end{cases}$$

If the eigenfunctions were orthogonal, then the integrals for these two cases would instead evaluate to $\frac{1}{2}$ and 0 respectively. For the specific case with $n = \ell = 1$, we find that

$$\int_0^1 \cos^2(\mu_1(y - 1)) \, dy \approx 0.4994,$$

while for $n = 1$ and $\ell = 2$

$$\int_0^1 \cos(\mu_1(y - 1)) \cos(\mu_2(y - 1)) \, dy \approx 3.701 \times 10^{-4}.$$

For larger values of $n$ and $\ell$, these integrals are even closer to the ideal values of $\frac{1}{2}$ and 0 and therefore the eigenfunctions are very nearly orthogonal. As a result, we are

able in practice to evaluate the series coefficients numerically by assuming that they are orthogonal and taking the short time solution to be

$$\gamma(y,\tau) = \frac{H\zeta + H \int_0^1 C_0(y)\,dy}{\zeta + H} + \sum_{n=1}^{\infty} a_n \cos\left(\mu_n(y-1)\right)e^{-\mu_n^2\tau}, \qquad (5.20)$$

where

$$a_n \approx 2 \int_0^1 (C_0(y) - \gamma_\infty) \cos\left(\mu_n(y-1)\right) dy, \qquad (5.21)$$

and $\mu_n$ are the roots of (5.19).

We remark here that a similar problem with an integral boundary condition has been studied by Beilin [1], who also looked for a series solution and obtained eigenfunctions that are not orthogonal. However, he carried the analytical solution further by deriving a second set of dual eigenfunctions for an associated adjoint problem that are orthogonal to the original eigenfunctions. He then used both sets of eigenfunctions to calculate the series coefficients analytically. We have not applied Beilin's approach here because our problem has a more complicated integral boundary condition that leads to a time-dependent boundary condition in the adjoint problem for which we cannot obtain eigenfunctions in the same way.

Finally, we note that contrary to the usual approach for developing matched asymptotic expansions, the short and long time expansions in our situation involve no unspecified constant(s) that require matching. In particular, the short time solution for the gas concentration tends to the constant function $\gamma_\infty$ as $t \to \infty$. This is also the steady state solution of the diffusion equation in the domain $0 \leqslant y \leqslant 1$ which coincides with the zeroth-order term in the long time expansion as $t \to 0$.

### 5.4 Comparison with numerical simulations

The asymptotic solution developed in the preceding sections is now calculated using the same parameter values that were used in the full numerical simulations shown in Figures 3–5, and the corresponding results are reported in Figures 8–10 respectively. In all cases, the short time series solution from (5.20) was truncated at 10 terms, while the long time expansion is depicted for both one- and two-term series approximations.

Focusing first on the base case results in Figure 8(b), for very short times the concentration solution is indistinguishable to the naked eye from the computed results. Over longer times, the temperature and two-term series expansions for both interfacial position and concentration (in Figures 8(a), (c) and (d) respectively) also sit directly on top of the computed results. The leading order concentration solution begins to deviate from the computed results when the boundary temperature difference is increased to $T_2 - T_1 = -2$ in Figure 10(b); this reduction in accuracy derives from the fact that the $G_0$ approximation is constant in space, whereas the actual concentration becomes more concave in $y$ as $T_2 - T_1$ increases. There is a more noticeable error in the leading order term for the interface position, which is most evident in Figure 9(a).

It is interesting to investigate the limitations of our asymptotic solution for more extreme values of the parameters and thereby determine under what circumstances the

(a) Temperature
(crosses – analytical solution).

(b) Gas concentration (short time)
(crosses – analytical solution).



(c) Water–ice interface.
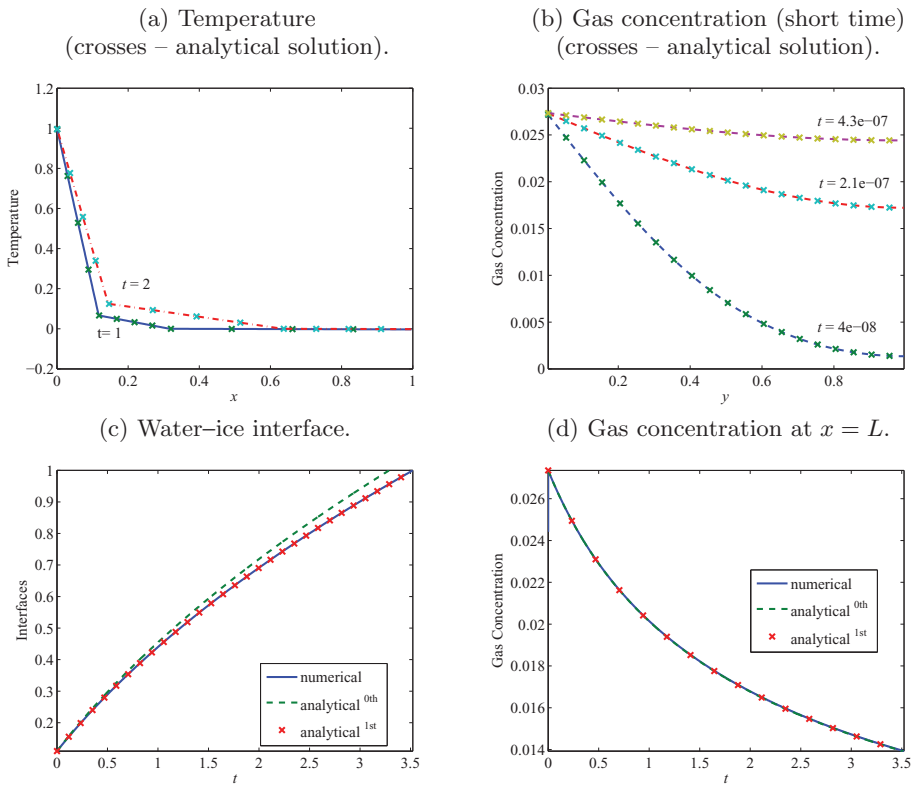
(d) Gas concentration at $x = L$.



FIGURE 8. (Colour online) Comparison of analytical and numerical solutions with boundary temperatures $T_1 = T_c + 0.005$, $T_2 = T_c - 0.005$, $\tilde{T}_2 = -1$.
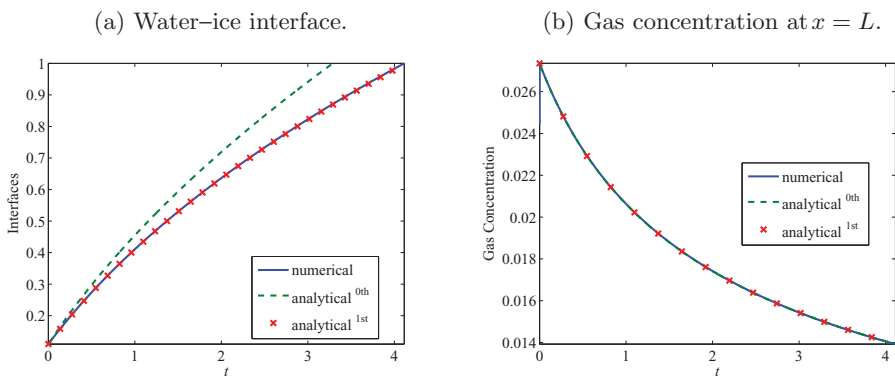
(a) Water–ice interface.

(b) Gas concentration at $x = L$.



FIGURE 9. (Colour online) Comparison of analytical and numerical solutions with boundary temperatures $T_1 = T_c + 0.005$, $T_2 = T_c - 0.02$, $\tilde{T}_2 = -4$.

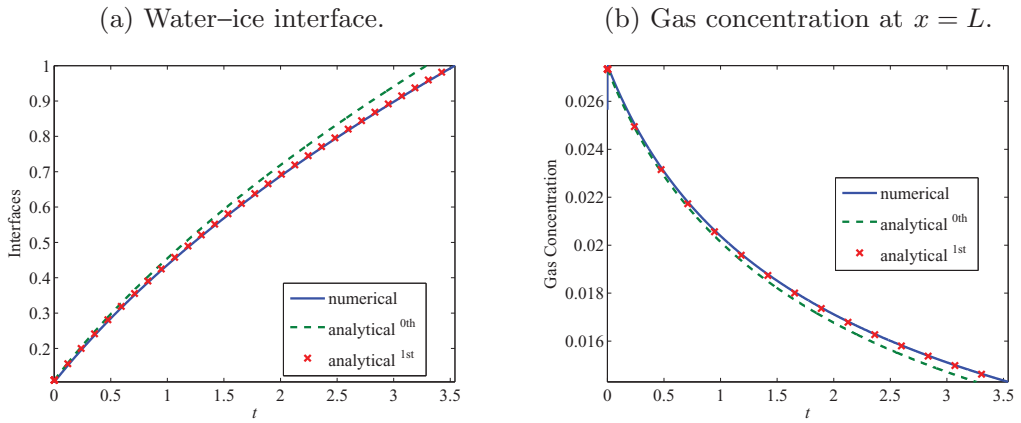(a) Water–ice interface.  (b) Gas concentration at $x = L$.



FIGURE 10. (Colour online) Comparison of analytical and numerical solutions with boundary temperatures $T_1 = T_c + 1$, $T_2 = T_c - 1$, $\tilde{T}_2 = -1$.
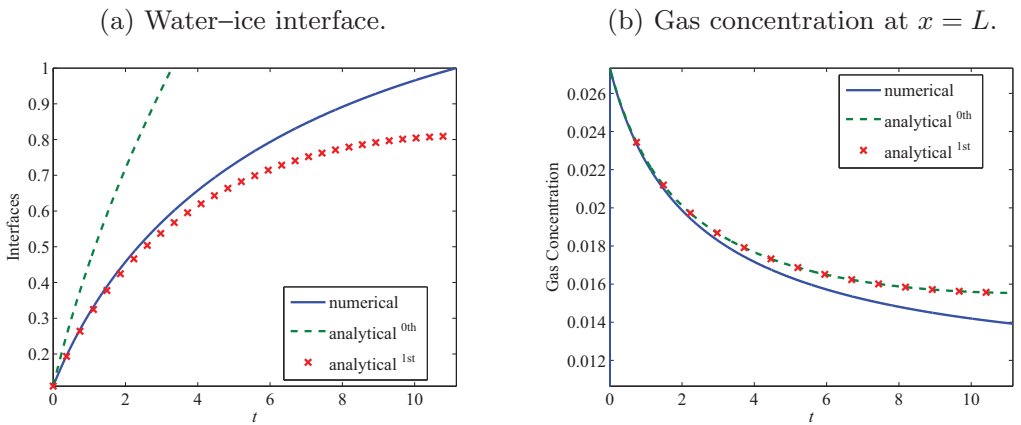
(a) Water–ice interface.  (b) Gas concentration at $x = L$.



FIGURE 11. (Colour online) Comparison of analytical and numerical solutions with boundary temperatures $T_1 = T_c + 0.005$, $T_2 = T_c - 0.005$, $\tilde{T}_2 = -1$ and $L = 1$ cm.

series begins to break down. For example, if the domain length is increased by several orders of magnitude to $L = 1$ cm, then there is finally a noticeable error in the two-term solution for concentration as shown in Figure 11(b); furthermore, the two-term asymptotic solution fails to adequately capture the interface position. Because it is only for such extreme values of parameters that the series approximation breaks down, we conclude that our approximate solutions remain accurate for the range of parameters corresponding to the melting of frozen sap in maple xylem cells.

# 6 Conclusions

In this paper we have developed a mathematical model for a three-phase free boundary problem that is motivated by the study of melting of frozen sap within maple trees. The model incorporates both melting of ice and dissolution of gas within the meltwater. We

derive an approximate solution that captures the dynamics of the ice–water interface as a series expansion in the Biot number. The dissolved gas concentration exhibits variations over two widely disparate time scales, leading to a two-scale asymptotic solution. Comparisons with numerical simulations show that the approximate solutions are accurate for a range of parameter values of interest in maple trees.

There are several possible avenues for the future work. Firstly, the gas–water interfaces within actual xylem cells experience a large curvature so that the interfacial surface tension will have a significant effect on pressure differences. We would like to include this effect, as well as the Gibbs–Thompson phenomenon for the variation of melting temperature across a curved interface which has been well studied in the mathematical literature [19]. Secondly, maple trees undergo repeated daily cycles of freezing and thawing, and so the freezing mechanism also needs to be analysed with a daily periodic variation in the temperature. Finally, we would like to study further some of the technical issues surrounding the extension of Beilin's approach [1] to the more complicated adjoint problem that derives from our integral boundary condition.

### Appendix A  Derivation of the gas–water interface equation (2.11)

Here we apply a conservation of mass argument to derive equation (2.11) relating $\dot{s}_{gw}$ and $\dot{s}_{wi}$, assuming that the domain is a cylinder with constant radius $r$. At any time $t$, the total mass of gas is given by the integral

$$\mathcal{M}_g(t) = A\left(\int_0^{s_{gw}(t)} \rho_g(s,t)\,ds + m_w(t)\right) = As_{gw}(0)\rho_g(0), \tag{A 1}$$

while that for water is

$$\mathcal{M}_w(t) = A\int_{s_{gw}(t)}^{s_{wi}(t)} \rho_w\,ds = 2A(s_{wi}(t) - s_{gw}(t))\rho_w \tag{A 2}$$

and for ice is

$$\mathcal{M}_i(t) = A\int_{s_{wi}(t)}^{L} \rho_i\,ds = 2A(L - s_{wi}(t))\rho_i. \tag{A 3}$$

As mentioned earlier, the water and ice densities are taken to be constant.

Since we assume that the system is closed, the sum of the three masses must be some constant, say $\mathcal{M}_0$, and so

$$\mathcal{M}_0 = \mathcal{M}_g(t) + \mathcal{M}_w(t) + \mathcal{M}_i(t). \tag{A 4}$$

Differentiating this expression with respect to time yields

$$0 = 0 + A(\dot{s}_{wi}(t) - \dot{s}_{gw}(t))\rho_w - A\dot{s}_{wi}(t)\rho_i, \tag{A 5}$$

or simply

$$\dot{s}_{gw}(t) = \left(1 - \frac{\rho_i}{\rho_w}\right)\dot{s}_{wi}(t). \tag{A 6}$$

## Appendix B Approximation of the eigenvalues $\mu_n$

Here we approximate the coefficients $\mu_n$ from equation (5.19) for small values of $H$. Then the integral boundary condition reduces to a pure Dirichlet condition and we then expect that the eigenvalues and eigenfunctions will reduce to those of the standard separation of variables solution. Indeed, if $\frac{H}{\zeta} = 0$ then equation (5.19) reduces to $\mu_n \cos(\mu_n) = 0$, whose solutions are $\{\mu_n^0 = (2n-1)\frac{\pi}{2},\ n = 1, 2, \dots\}$. Because we are interested in the case when $\frac{H}{\zeta}$ is very small, we can make the ansatz $\mu_n = \mu_n^0 + \epsilon_n$ with $\epsilon_n \to 0$, and assume further that $|\sin(\mu_n)| \approx 1$. As a result, equation (5.19) becomes

$$|\mu_n| \cdot |\cos(\mu_n)| \approx \frac{H}{\zeta}. \tag{B 1}$$

Using the Taylor series expansion of the cosine function centred at $\mu_n^0$, (B 1) reduces to

$$\epsilon_n^2 + \mu_n^0 \epsilon_n - \frac{H}{\zeta} = 0, \tag{B 2}$$

resulting in

$$\epsilon_n = \frac{1}{2}\left[\sqrt{(\mu_n^0)^2 + \frac{4H}{\zeta}} - \mu_n^0\right] = \frac{\mu_n^0}{2}\left[\sqrt{1 + \frac{4H}{\zeta(\mu_n^0)^2}} - 1\right]. \tag{B 3}$$

Finally, we employ the approximation

$$\sqrt{1 + z} = 1 + \frac{z}{2} + o(z)$$

to obtain

$$\epsilon_n \approx \frac{\mu_n^0}{2}\left[1 + \frac{2H}{\zeta(\mu_n^0)^2} - 1\right] = \frac{H}{\zeta \mu_n^0} \tag{B 4}$$

so that

$$\mu_n = (2n-1)\frac{\pi}{2} + \frac{2H}{\zeta(2n-1)\pi}. \tag{B 5}$$

## References

[1] BEILIN, S. A. (2001) Existence of solutions for one-dimensional wave equations with nonlocal conditions. *Electron. J. Diff. Equ.* **2001**(76), 1–8.

[2] CARSLAW, H. S. & JAEGER, J. C. (1988) *Conduction of Heat in Solids*, 2nd ed., Clarendon Press, New York, NY.

[3] CESERI, M. & STOCKIE, J. M. (2013) A mathematical model of sap exudation in maple trees governed by ice melting, gas dissolution, and osmosis. *SIAM J. Appl. Math.* **73**(2), 649–676.

[4] COHEN, D. S. & ERNEUX, T. (1988) Free boundary problems in controlled release pharmaceuticals. I. Diffusion in glassy polymers. *SIAM J. Appl. Math.* **48**(6), 1451–1465.

[5] CRANK, J. (1956) *The Mathematics of Diffusion*, Clarendon Press, New York, NY.

[6] CRANK, J. (1984) *Free and Moving Boundary Problems*, Clarendon Press, New York, NY.

[7] EVANS, J. D. & KING, J. R. (2000) Asymptotic results for the Stefan problem with kinetic undercooling. *Quart. J. Mech. Appl. Math.* **53**(3), 449–473.

[8] FRIEDMAN, A. (1959) Free boundary problems for parabolic equations. I. Melting of solids. *J. Math. Mech.* **8**, 499–517.

[9] FRIEDMAN, A. (1960) Free boundary problems for parabolic equations. III. Dissolution of a gas bubble in liquid. *J. Math. Mech.* **9**, 327–345.

[10] FRIEDMAN, A. (1982) *Variational Principles and Free-Boundary Problems*, John Wiley, New York, NY.

[11] FRIEDMAN, A. (2000) Free boundary problems in science and technology. *AMS Not.* **47**(8), 854–861.

[12] FURZELAND, R. M. (1980) A comparative study of numerical methods for moving boundary problems. *J. Inst. Math. Appl.* **26**(4), 411–429.

[13] GUPTA, S. C. (2003) *The Classican Stefan Problem: Basic Concepts, Modelling and Analysis*, North-Holland Series in Applied Mathematics and Mechanics, Vol. 45, Elsevier, Amsterdam, Netherlands.

[14] HUANG, W. & RUSSELL, R. D. (2011) *Adaptive Moving Mesh Methods*, Applied Mathematical Sciences, Vol. 174, Springer, New York, NY.

[15] HUYAKORN, P., PANDAY, S. & WU, Y. (1994) A three-dimensional multiphase flow model for assesing NAPL contamination in porous and fractured media, 1. Formulation. *J. Contam. Hydrol.* **16**(2), 109–130.

[16] KELLER, J. B. (1964) Growth and decay of gas bubbles in liquids. In: *Proceedings of the Symposium on Cavitation in Real Liquids (General Motors Research Laboratory, Warren, MI)*, Elsevier, New York, NY, pp. 19–29.

[17] KING, J. R. (1986) *Mathematical Aspects of Semiconductor Process Modelling*. D. Phil. thesis, Oxford University, Oxfprd, UK.

[18] KONRAD, W. & ROTH-NEBELSICK, A. (2003) The dynamics of gas bubbles in conduits of vascular plants and implications for embolism repair. *J. Theor. Bio.* **224**, 43–61.

[19] LUCKHAUS, S. (1990) Solutions for the two-phase Stefan problem with the Gibbs–Thomson Law for the melting temperature. *Euro. J. Appl. Math.* **1**, 101–111.

[20] MILBURN, J. & O'MALLEY, P. (1984) Freeze-induced fluctuations in xylem sap pressure in *Acer pseudoplatanus*: A possible mechanism. *Can. J. Bot.* **62**, 2100–2106.

[21] MITCHELL, S. L. & VYNNYCKY, M. (2009) Finite-difference methods with increased accuracy and correct initialization for one-dimensional Stefan problems. *Appl. Math. Comput.* **215**(4), 1609–1621.

[22] PLESSET, M. S. & PROSPERETTI, A. (1977) Bubble dynamics and cavitation. *Annu. Rev. Fluid Mech.* **9**, 145–185.

[23] SINGH, K. & NIVEN, R. K. (2013) Non-aqueous phase liquid spills in freezing and thawing soils: Critical analysis of pore-scale processes. *Crit. Rev. Environ. Sci. Technol.* **43**(6), 551–597.

[24] TAO, L. N. (1979) On solidification problems including the density jump at the moving boundary. *Quart. J. Mech. Appl. Math.* **32**(2), 175–185.

[25] TSYPKIN, G. G. (2000) Mathematical models of gas hydrates dissociation in porous media. *Ann. New York Acad. Sci.* **912**(1), 428–436.

[26] Tyree, M. T. & Sperry, J. S. (1989) Vulnerability of xylem to cavitation and embolism. *Annu. Rev. Plant Physiol. Plant Mol. Biol.* **40**, 19–38.

[27] Wilson, D. G. (January 1982) *One Dimensional Multi-Phase Moving Boundary Problems with Phases of Different Densities.* Technical Report CSD-93, Oak Ridge National Laboratory, Oak Ridge, TN.

[28] Xu, W. (2004) Modeling dynamic marine gas hydrate systems. *Am. Mineral.* **89**(8–9), 1271–1279.